Optimal site selection for Choutuppal geomagnetic observatory, based on geophysical evidences

Divyanshu Dwivedi[1], Sneh Yadav[2], Kusumita Arora[1], Rakesh Murteli[1], Alok Taori[3]
[1]Geomagnetism, CSIR-National Geophysical Research Institute, India
[2]Kurukshetra University, India
[3]National Remote Sensing Centre, India
Correspondence: Divyanshu Dwivedi; email id: ddwivedigp@gmail.com

Abstract

The phases of development ~~of the stages~~ of the Choutuppal magnetic observatory over last 15 years has enabled the effects of the natural environment like groundwater changes and lightning activity on the magnetic data to be evaluated. A ~~new~~ high resolution survey ~~for~~ of total field anomalies led to the construction of the 3D model of the shallow surface. ~~and analysis of lightning data is carried out to understand the nature of the subsurface. Based on model from high resolution magnetic data and~~Constrained by conductivity depth slices from previous ERT and EVRI surveys, the distribution of sandy regolith, saprolite, and granitic layers in the shallow subsurface ~~to be~~are delineated. The pattern of lightning strikes in a 10 km area around the observatory are correlated to modulations and disruptions in the magnetic data. ~~This~~ The ~~model~~ analysis as a whole provides information for selecting a location to install ~~the magnetic observatory~~a secondary variometer room by taking into account topography, lightning effect, soil resistivity, low magnetic ~~gradients~~ anomaly ~~,~~and distance from the recharge pond, which can produce continuous data of higher quality and consistency than at present.

Keywords: Choutuppal observatory, Magnetic anomaly, Spectral analysis, Lightning data

1. Introduction:

The Choutuppal (CPL) geo-electric observatory (Geographic coordinates: 78.920E, 17.290N; Geomagnetic coordinates: 149.24E, 7.47N) of CSIR-NGRI was established near Choutuppal town in the Nalgonda district, approximately 60 km southeast of Hyderabad city, Telangana state (Sanker Narayan, 1964). The region primarily comprises granite and gneissic formations. These rocks are part of the Peninsular Gneissic Complex, which is one of the oldest geological formations in India, dating back to the Archean era. The weathering of the granitic and gneissic rocks has led to the formation of red and lateritic soils. The granitic formation is encroached locally by discontinuities such as dikes or quartz reefs but these are not present on the site (Guihéneuf ~~Guiheneuf~~ et al., 2014). The area around the CPL observatory mainly consists of alkali feldspar granite (Figure 1a). The regional geology of resistive granitic basement rocks, uniform soil cover, arid vegetation, and gentle topography for effective drainage of runoff water during rainy seasons were assessed to be suitable for geo-electric measurements (Sankear Narayan et al., 1967; Sarma et al., 1969). Below the surface, shallow drillings revealed: 1) A sandy regolith layer 0-2 m thick which is made up of sandy-clay of quartz grains, 2) A laminated saprolite layer of variable thickness of 10 -15 m derived from in-situ weathering of granite, 3) A 15-20 m thick layer of fissured granite, where weathered granite and some clay partially fill the fissures. The effective porosity of this layer is very low and mainly due to the fissure zones (Dewandel et al., 2006; 2012).

~~A topographic and magnetic survey was conducted in the region.~~ The geo-electric measurements at CPL were based on orthogonal 500 m electric dipoles and magnetic pulsations were measured with solid core induction coils. Hourly values of the

59   magnetic variation and analysis of equatorial magnetic pulsations were reported from

60   CPL (CSIR NGRI report, 1972). These hourly values are published in the Indian

61   magnetic data volumes and uploaded to WDC Kyoto (Svendsen et al., 1990). Figure

62   1b shows the 105 acre star shaped campus of CSIR-NGRI in Choutuppal. One high

63   magnetic anomaly is present at the eastern part of the campus. In the rest of the area,

64   the total range is ~ about 80 nT. The surface topography is least in the east and north

65   and highest higher is the west and southern part of the campus. Several shallow

66   boreholes drilled in the northern end are used for hydrogeological studies in fractured

67   hard rock terrains. These studies monitored the nature of the granitic basement rocks,

68   local hydrogeology, and groundwater managed aquifer recharge (MAR) within the CPL

69   observatory, through a large, shallow lake in the eastern quadrant of the campus.

70

71   Geo-electric measurements on this campus were discontinued in 1982—, but

72   Consequent to when the Metro Rail project in the vicinity of the HYB magnetic

73   observatory in Hyderabad appeared to threaten its existence in 2010, the Choutuppal

74   campus was re-visited for re-location possibilities of HYB. This work showcases

75   summarizes the different situations, which affect the operation of a low latitude

76   magnetic observatory, some mitigation measures and some unanswered questions.

77

78

79

80
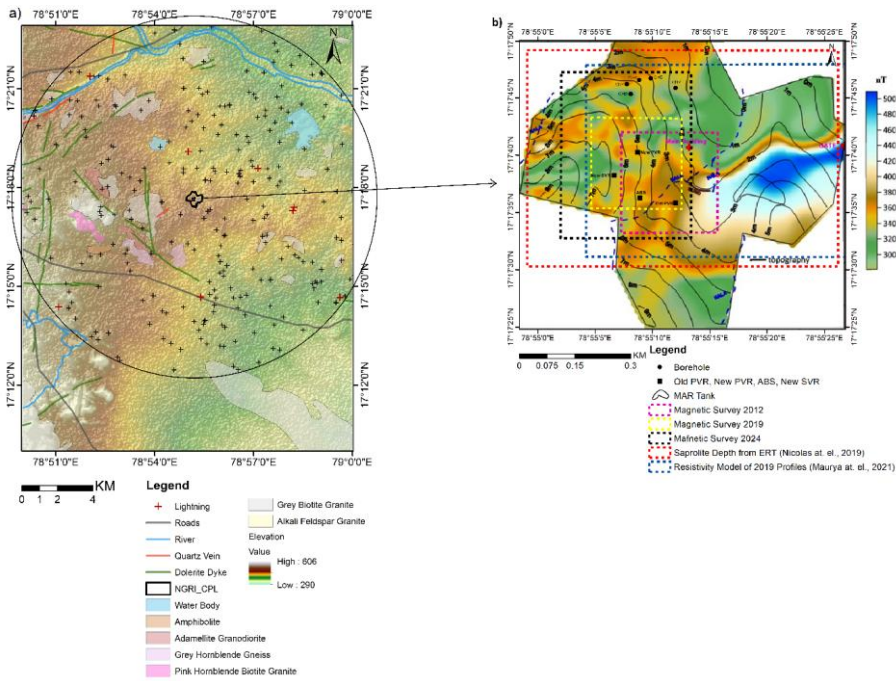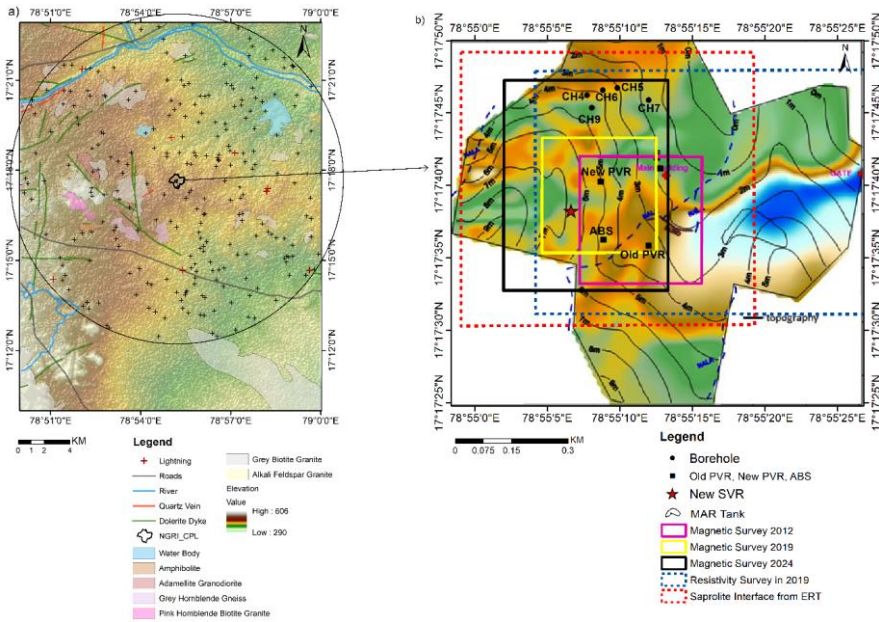
81 **Figure 1:** a) The geological map shows the area around the CSIR-NGRI- CPL
82 observatory superimposed over topography. ~~(SRTM Global 30 meter) situated on~~
83 ~~alkali feldspar granite, plus~~ '+' symbols show lightning locations within a 10 km radius
84 (circle mark) from January 2022 to August 2022 with maximum intensity 60480 amp,
85 b) The magnetic anomaly map (after Sanke~~hanka~~r Narayan et al., 1967) is
86 superimposed ~~over the~~on local elevation. ~~with marked area of previous studies~~The
87 locations of the magnetic and electric surveys are marked by solid and dashed
88 rectangles. PVR=Primary variometer room. ~~, NV=New Vault~~, ABS= Absolute room,
89 SVR= Secondary variometer room. MAR = managed aquifer recharge.
90 ~~.~~
91

92 **2. First phase of CPL Magnetic Observatory:**

93 **i)   Survey of magnetic data ~~gradients~~ and building CPL Observatory**
94
95 Prior to establishing the observatory buildings, a magnetic survey was conducted in

96 November 2012 over an area of 200 m x 200 m with 20 m intervals, between the Main

97 ~~building~~ Building and the southern side of the campus, marked by pink ~~dotted~~

98 ~~line~~rectangle in Figure 1b, which ~~appeared to be have~~had the smallest ~~anomalies~~

99 ~~gradients~~anomalies ~~from~~as per the earlier survey. This area was sufficiently far away

100 from the boundary of the campus to ensure that local activities outside the campus

101 may not have significant contribution to the measurements. The total magnetic

102 anomaly range (Figure 2) was ~ 150nT with changes in magnetic field within ~20 nT

103 around proposed locations of the ~~old~~ oOld PVR and ABS rooms.
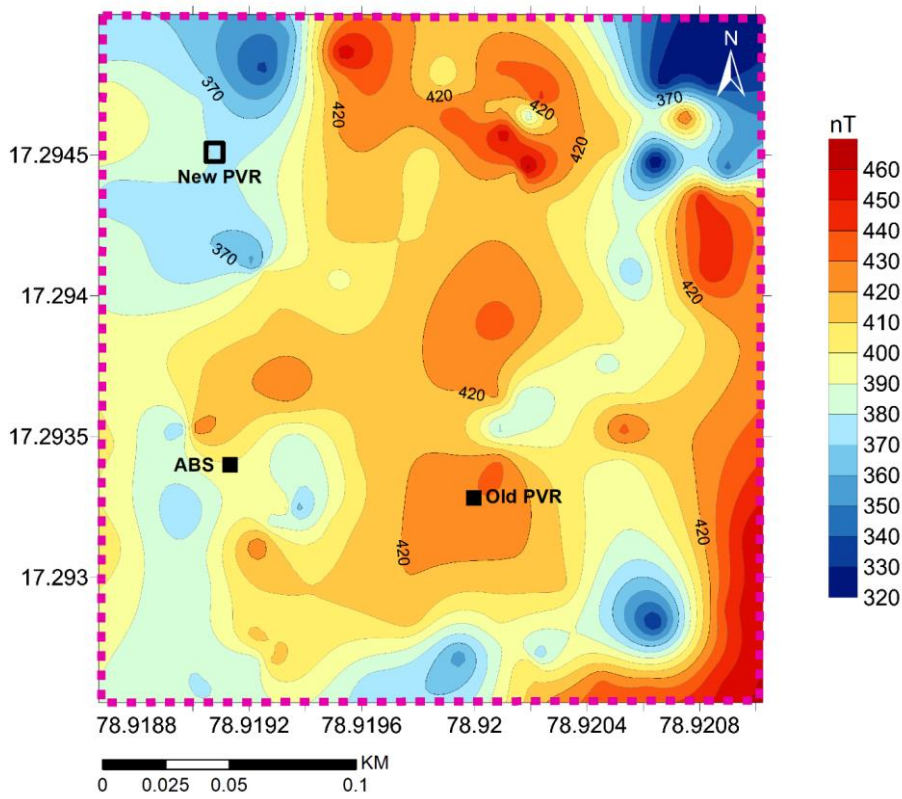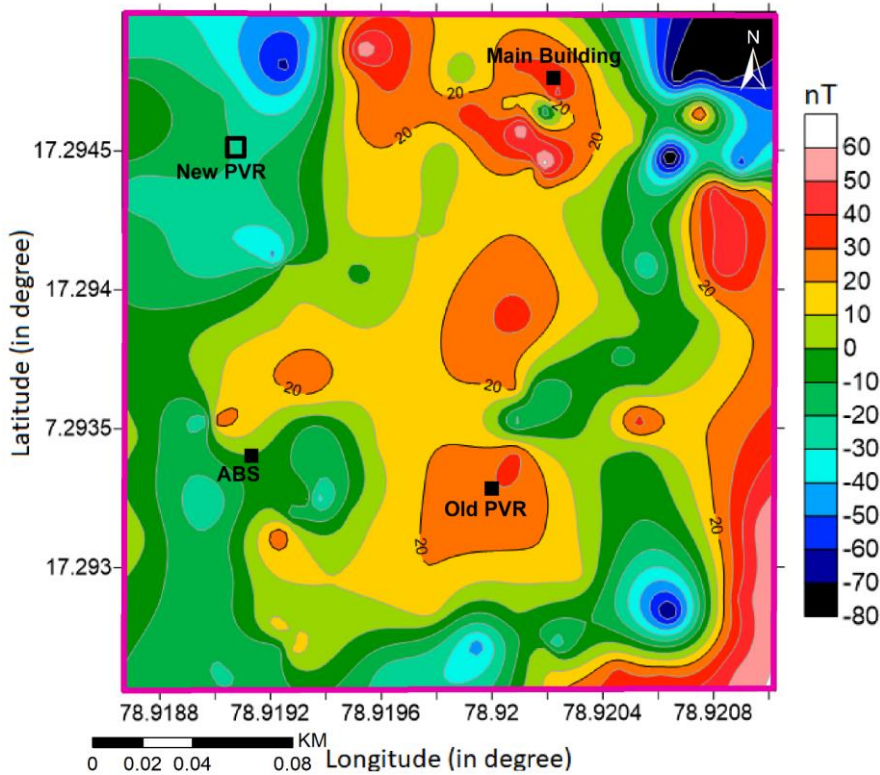
Figure 2: Magnetic anomaly plot of the survey region in 2012. Black box is the marked location for the New PVR, built in 2019-2020. Main Building to be marked on map

In this central location the surface topography was moderatelyis low and a shallow water channel (nalla) flowed flows SE-NW through the area between the Old PVR and ABS. The old Old PVR construction (with double walled, 3.5 m underground vault) started in the June 2013 using non-magnetic sandstone. The ABS room was constructed on slightly elevated ground with two pillars inside and four pillars outside. In April 2014, the CPL observatory was commissioned, equipped with tri-axial fluxgate magnetometer and Zeiss single axis fluxgate theodolite for Declination-Inclination measurements. The XVII IAGA Observatory Workshop was held on this these

117   premises in October 2014 with 93 international participants from 33 countries. The

118   definitive data from CPL is published at INTERMAGNET, 2015 onwards.

119

120   **ii)   Hydrogeological Park and managed aquifer recharge:**

121   The region of CPL Observatory has a semi-arid climate with an average annual

122   maximum temperatures ranging as 28°C - 45°C. The mean annual rainfall is around

123   751 mm, which ranges from 2 mm in February to 171 mm in July. Water levels are

124   highly variable depending on the monsoon and usually range between 2 and 26 m

125   (meters below ground surfacegs). Water level measurements at the northern part of

126   the Choutuppal campus has been monitored since 1999 in two dozen boreholes, some

127   of them are marked shown in Figure 1b, by the Indo-French Center for Groundwater

128   Research (IFCGR) (Maréchal Mareschal et al, 2018) to study the hydrodynamic

129   properties and associated hydrological processes in crystalline aquifers. As part of a

130   governmental scheme of strengthening groundwater through recharge state-wise

131   MAR projects, an infiltration basin was dug in Choutuppal (marked in black outline as

132   MAR in Figure 1b) during in 2015 to meet the demands of farmers in the area

133   facing water scarcity. The basin has dimensions of 120 m × 40 m, with a depth of about

134   2 m, effectively removing the regolith layer and extending into the saprolite. The basin

135   is mainly supplied by a canal which deviates diverts water from the Musi River .

136   (Nicolas et al., 2019; Maurya et al., 2021) and was first filled in 2015. Nicolas et al

137   (2019) has shown that intra-seasonal groundwater fluctuations have only moderate

138   response to rainfall patterns, which could be due to usage trends as well as hydraulic

139   permittivity parameters. After the MAR basin filling, groundwater levels rose by 6 m in

140   one year. Figure 3a shows the water level changes of five boreholes (CH5, CH4, CH6,

141   CH7, and CH9) before and after monsoon from 2011 to 2023 with a data gap during

142 2021-22. While it is clear that most of the time water level lies at intermediate depth of

143 ~ 10 to 30 m, individually, CH5 and CH7 show the least seasonal fluctuations over the

144 years, CH6, CH4 and CH9 show variations of 20 m or more; possibly very local fracture

145 properties facilitate vertical flow of ~~downward seepage of~~ water ~~preferentially~~. Starting

146 from April 2017, the water levels in the boreholes rose significantly, coming almost to

147 surface in September 2017 and reducing a little by July 2018. In December 2023, the

148 water levels recorded are nearly similar to that of September 2017. It can be inferred

149 that sustained water in the MAR basin has allowed the shallow aquifers to be

150 permanently recharged. In September 2017, the rainfall of the monsoon combined

151 with prevalent saturated condition led to the flooding of the ~~magnetometer room~~Old

152 PVR vault . ~~The vault of the PVR rose nearly to surface and damaged the fluxgate~~

153 ~~magnetometer and electronics~~ (Figure 3cb). The water level receded by a few metre

154 the following summer but did not fall to earlier levels. While this was good news for

155 recharge, the Old PVR was ~~made~~ now unusable.

156

157
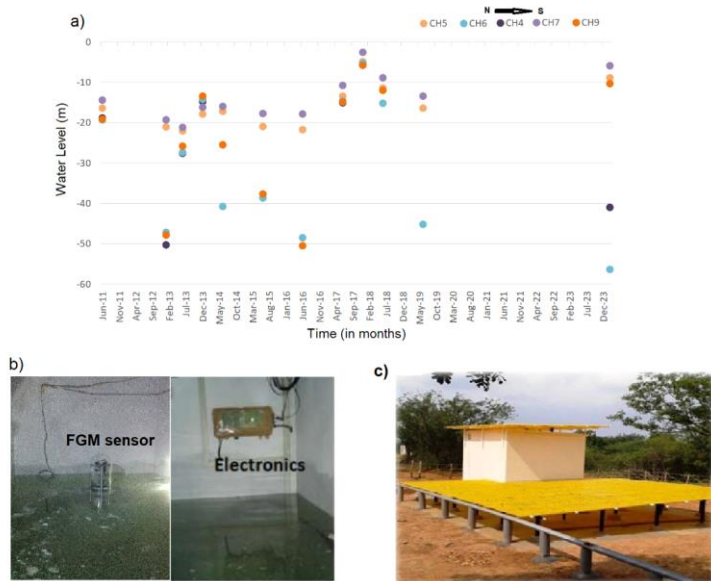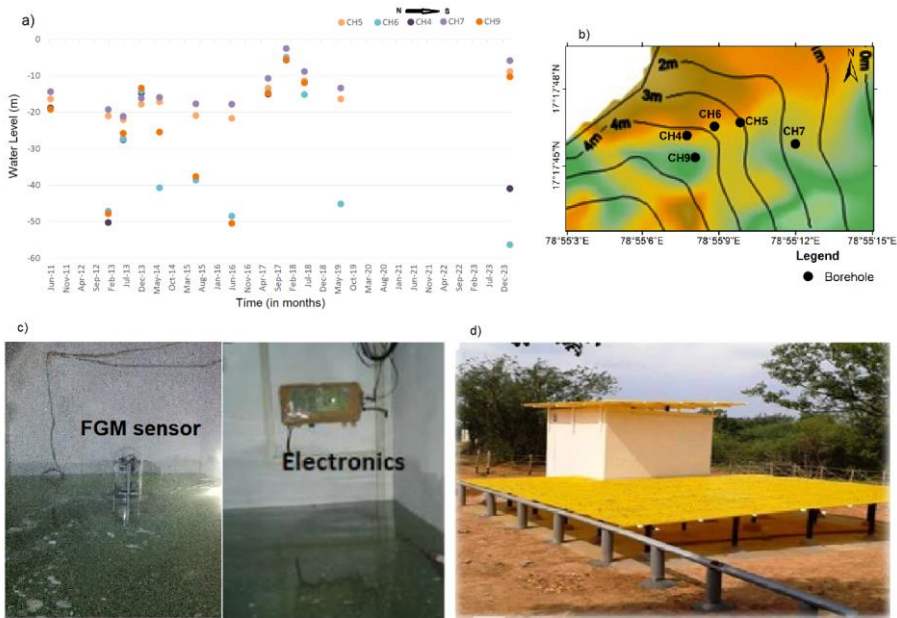
Figure 3: a) Fluctuations of water level in a few boreholes in the north of Choutuppal campus, b) location of boreholes in the map, cb) the submerged vault

in September 2017, de) the outside view of the old PVR. ~~Include an enlarged pic of the boreholes in map~~

3. Second phase of CPL Magnetic Observatory:

i)   Survey and commissioning of new PVR

With the need for a new variometer building, a fresh survey was conducted in May 2019 using GSM19 Overhauser magnetometers, marked by the yellow ~~dashed box~~rectangle in Figure 1b. This area was some tens of meter west of the earlier survey location, still central to the campus, on ground which is about 2-3 m higher, which could avoid the shallow groundwater conditions. This total field magnetic survey was carried out during six ~~days (~~geomagnetic quiet days~~)~~ in May 2019 over a 240 X 240 square meter area with 10 m spacing. The magnetic anomaly of the region shows total amplitude variation of ~300nT (Figure 4a) with ~10nT anomaly north of the ABS room; the proposed location is marked as New PVR in Figure 4a. This time a raised building with double walls and double roof was constructed of non-magnetic limestone to ensure no groundwater incursion issues for the foreseeable future (Figure 4b). The New PVR was commissioned in January 2021.
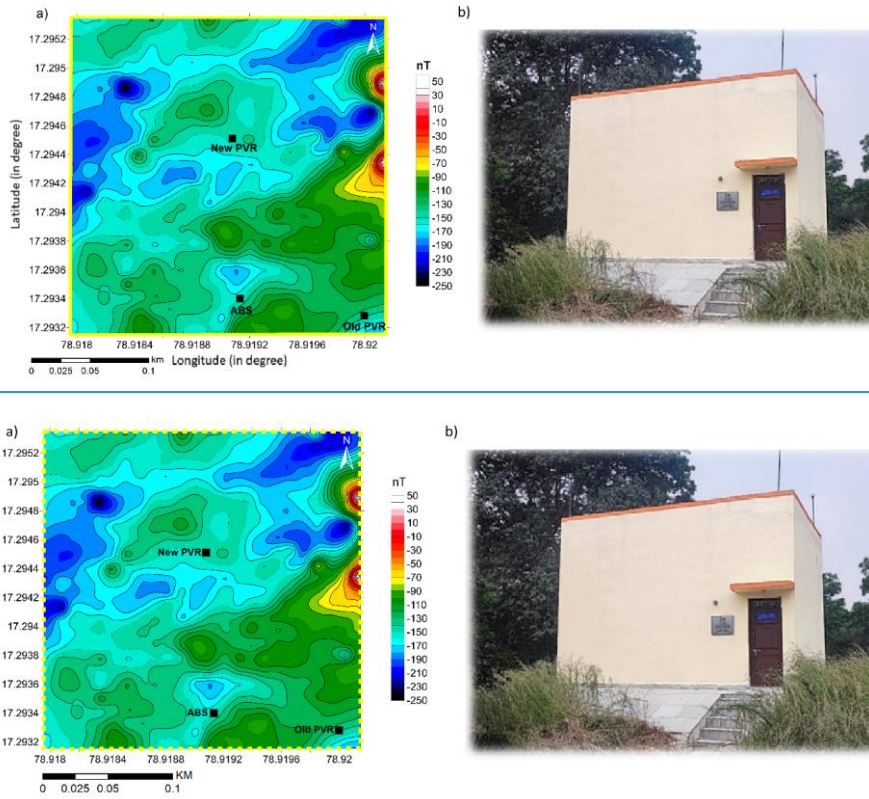
Figure 4: a) Magnetic anomaly plot of the survey region in 2019, b) New PVR building inaugurated in January 2021.

Recurrent malfunctions of the electronics (2-3 times a month) of the digital fluxgate magnetometer (DFM) recording ~~system~~ electronics were noticed in second half of 2021 and 2022, a new phenomenon. After rounds of thorough inspections, ~~These incidences were later correlated with~~it was suspected that lightning activity in the vicinity of the Choutuppal campus was causing the damage inspite of installation of 6 lightning arrester rods and 4 earthing pits. Being an open ground with no tall obstructions, the lightning activity in this area was found to be more frequent than

194 around HYB observatory in Hyderabad. ~~Strengthening of t~~The earthing pits and
195 lightning arrester system were strengthened further but only marginally countered the
196 effects on the electronics.

197

198 **ii)   Lightning activity patterns around CPL Observatory and effects on**
199 **data**

200 ISRO-National Remote Sensing Center (NRSC) has a network of 46 radio
201 frequency~~27 VLF~~ lightning detection sensors, covering the ~~southern~~ entire part of the
202 India ~~country~~ (shown in Figure 5a). The Lightning detection sensor network monitors
203 the cloud to ground lightning occurrences by virtue of emitted waves in the 5 Hz - 30
204 MHz range and geolocation is calculated using the time of arrival method. The
205 detection range is upto 800 km with more than 98% confidence within 300 km range,
206 with 50% overlap to maintain high geo-location accuracy of lightning occurrences ~~The~~
207 ~~detection range is upto 800 km with more than 98% confidence within 300 km range,~~
208 ~~with 50% overlap to maintain high geo-location accuracy on the recent past which may~~
209 ~~be due to the induced current generated in the subsurface~~(Taori et al., 2022; 2023).
210 We have examined the lightning data in a radius of 10 km around CPL observatory,
211 marked as + in Figure 1a. Figure 5b shows the ~~shows the~~ occurrence frequency of
212 lightning over the months from January to August 2022; + symbols denote the
213 instances when the lightning caused damage in the fluxgate electronics. Figure 5b
214 shows that substantial lower intensity lightning activities are recorded during January,
215 April, May and June. Surprisingly July had no lightning in the area in 2022, in August,
216 the higher intensity lightning were more numerous. Two instances of failure of the
217 instrument electronics occurred during the higher intensity lightning of April and

218 August, whereas a disturbance of May was associated with lower amplitude lightning,

219 discussed in next section.
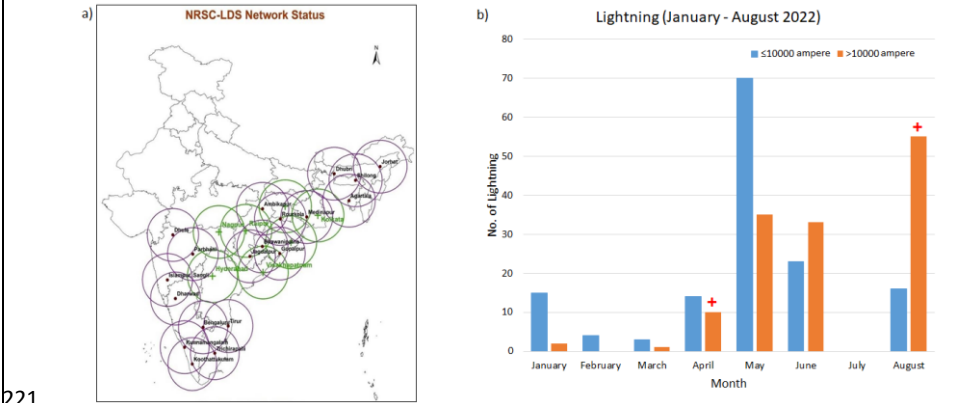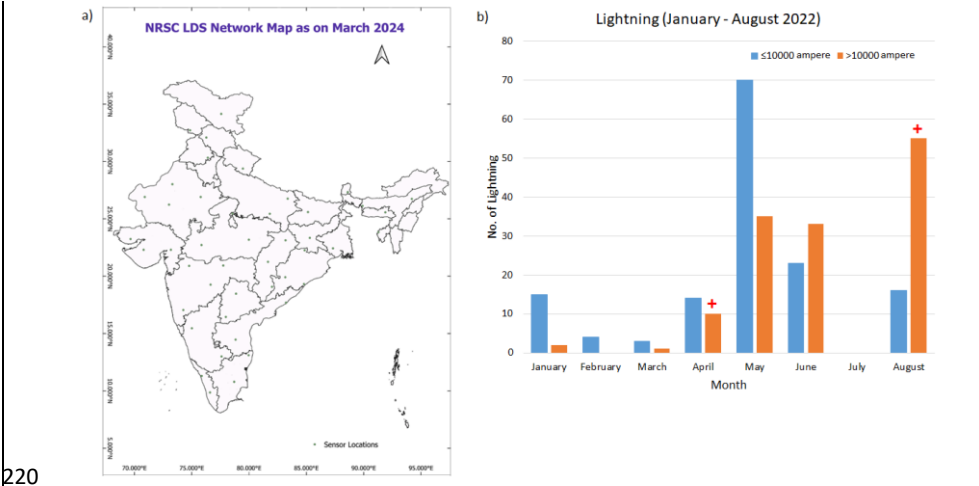
Figure 5: a) Map of lightning sensors in India, **b)** Distribution of low and high intensity
lightning occurrences during January to August 2022.

227 Examination of the H (horizontal), D (declination), and Z (vertical) components of 1-

228 sec data in LT (local time) for 04th May, 2022 data from the new PVR shows continuous

229 spikes from 7- 8.2 LT in all the components, followed by a shift of ~ 70, 20 and 150 nT

230   in H, D and Z respectively (Figure 6a). After rebooting the instrument, the data came

231   back to its normal range. Comparison with lightning data established that this

232   disturbance was due to lightning effect (correlated red mark). It is noticed that at the

233   time of 7.94 LT hour there was shift in the data which correlate with the lightening

234   intensity of 8879 amps and 14243 amps at the same time (Lightning data from NRSC)

235   which strike the ground within 10 km radius of CPL campus.

236

237
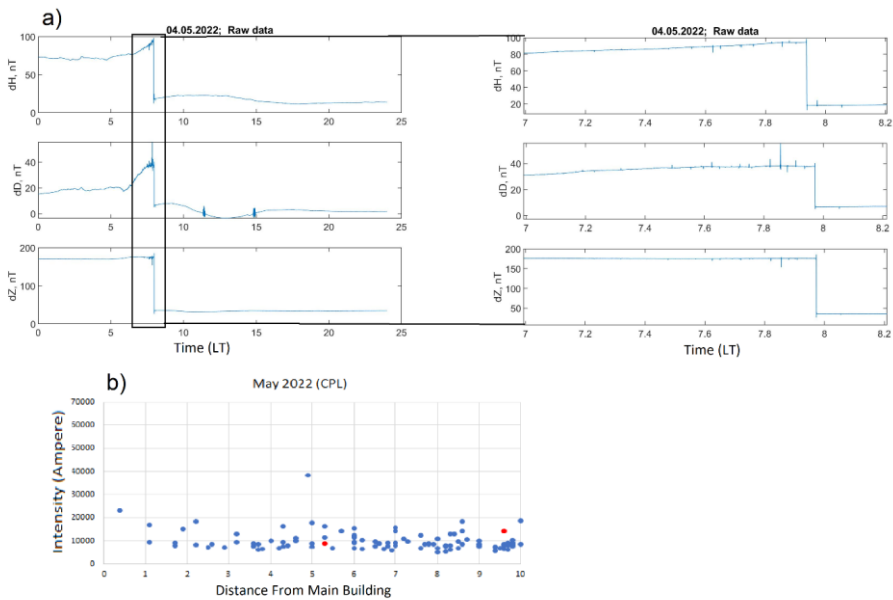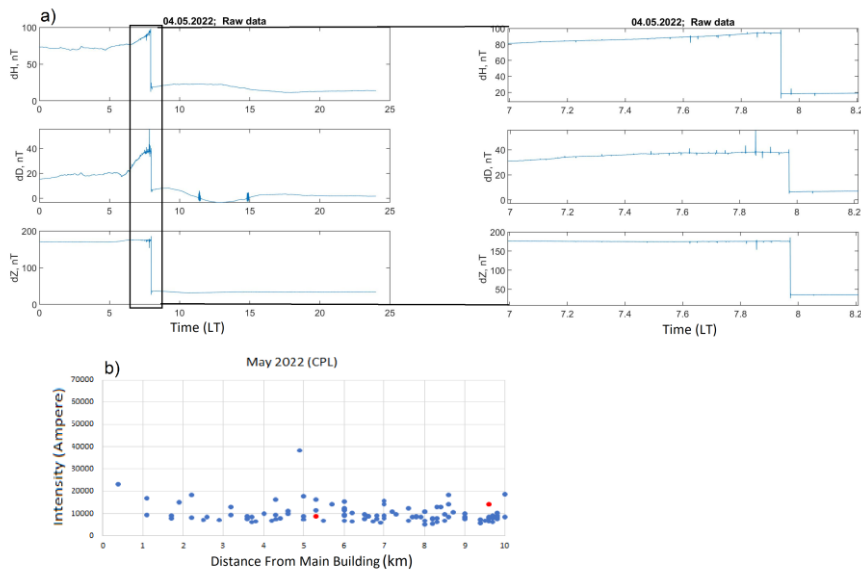
Figure 6: Raw data (H, D, Z component) plot for a) 04ᵗʰ May, 2022 at the new PVR, b) plot of lightning intensity (in ampere) with distance (in km) from main building.

Further, we examined the H, D, Z components of 1-sec data in LT or the 30ᵗʰ April and 26ᵗʰ May, 2017 data from the Oeld PVR, on days which had some weather activities. From the data, it is clear that there were no shifts in the data, but some continuous spikes were observed from 18.0 -18.8 LT (Figure 7). The spikes are more prominent in the Z component (>0.5nT). Though lighting data was not available in this duration, the general conditions lead us to believe that these minor signatures were lightning induced.
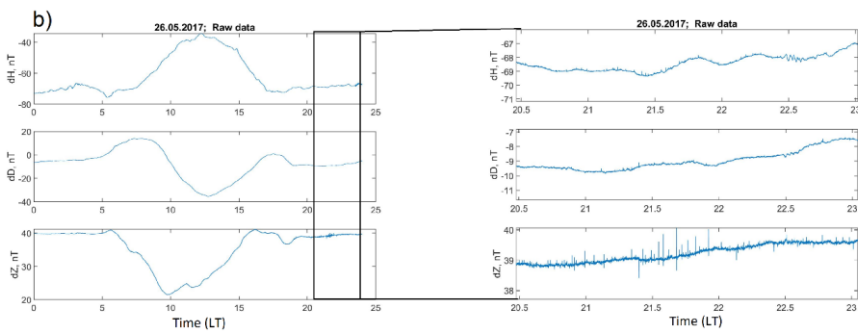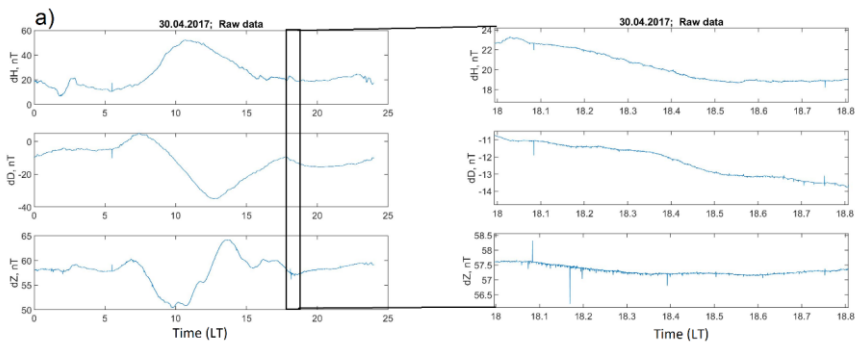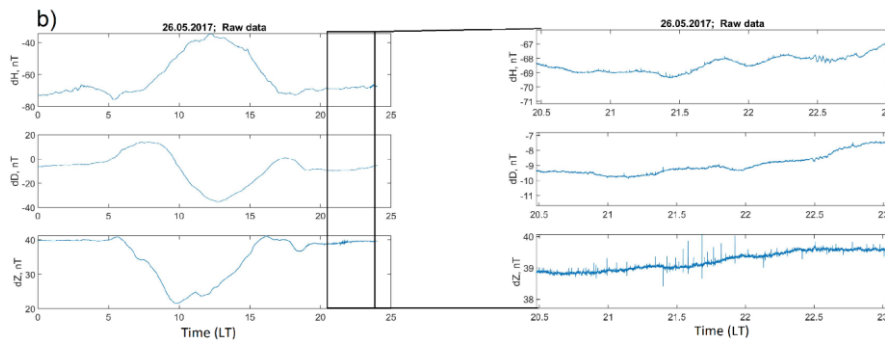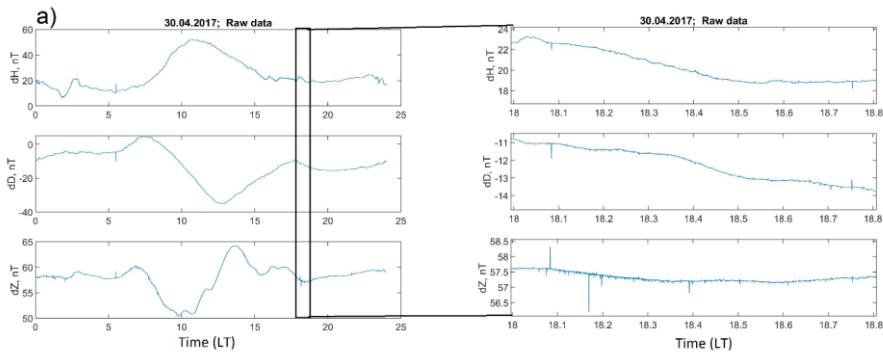
is-

Date	Time (LT)	H	D	Z	Lightning amplitude (ampere)	Distance (km)	Remark
15-04-2022	23.2 - 24.00	0.1nT	0.2nT	1nT	20968	5.5	GSM90 stopped recording & spikes in HDZ
04-05-2022	7.0 - 8.2	70nT	20nT	150nT	8879, 14243	5.3, 10	Shift in data(HDZ)
29-08-2022	-	-	-	-	37387,24329, 21210, 8553	3.9, 5.5, 9.2, 10	DFM Stopped recording
30-04-2017	18.0 - 18.8	0.8nT	1nT	1.2nT	-	-	Spikes in HDZ
26-05-2017	20.5 -23.0	0.2nT	0.2nT	1nT	-	-	Spikes in HDZ

271
272

273
274
275
276
277

278

279

280 It can inferredwas suspected that because the location of the new PVR is

281 constructuedconstructed on the surface and the cables as well as fact that the pillars

282 and infrastructure were installedwere laid in the surface layer, instead of the3-4 m

283 deeper vault configuration as in the one which was flooded, has amplified the effects

284 of lightning activity on the data has been amplified. Given the fact that in future years

285 more uncertainty and swings in climatic parameters are anticipated due to effects of

286 climate change, it was deemed necessary to conduct further studies to find a location

287 based on optimal ranges of a variety of parameters like topography, distance from

288 MAR lake, the configuration of near surface regolith and saprolite layers along with

289 groundwater conditions.

290

291 **4. New search for optimal location**

292 Higher ground away from the MAR basin can be found toward the western side of the

293 campus. In order to evaluate its suitability as a new long term location for continuous

294 magnetic measurements, This this study aims to delineate the sub-surface structures

295 using the high-resolution magnetic data in combination withconstrained by resistivity

296 information conducted through Electrical Resistivity Tomography (ERT) and Electrical

297 Vecrtor Resistivity Imaging (EVRI) measurements at the Choutuppal campus and

298 surrounding areas during 2016-2017. The magnetic method can be sensitive to

299 presence of near surface variations and produce a model of these layers as well as in

300 locating faults, folds, shear zones, delineating geological structures, and groundwater

301 contamination studies (Reynolds, 1997; Hinze et al., 2013; Kumar et al., 2018; Dwivedi

302 and Chamoli, 2021, 2022). Finally, wWe try to find out a suitable location called for a

303 new SVR (secondary variometer room) where effects of lightning and groundwater

304 level changes can be minimum in the medium-to-long term.

305

306 **i)   2024 survey**

307 A 1-sec total magnetic field survey was conducted during February 2024 (4 days) at

308 10 m sampling intervals as same done in 2019 survey. The data of 2019 and 2024

309   were combined, thus covering a total of ~ 400x320 square meters. The diurnal and

310   International Geomagnetic Reference Field (IGRF 14) corrections are applied to the F

311   data, so that the residuals reflect only the local crustal contributions. Finally, we applied

312   the kriging interpolation method to generate the grid and produce the magnetic

313   anomaly of this area (Figure 8a). Further, this was converted by a 'reduced to equator'

314   computation to remove ambiguities in location of causative sources of magnetic

315   anomalies, at low and high latitudes. In this study, we chose the values of

316   Delineation=0°, and Inclination=24° and estimate the RTE generated magnetic

317   anomaly map of the study region. The RTE filtered map centres anomalies over their

318   sources and removes the asymmetry of the magnetic anomaly due to nonzero

319   magnetic inclination and helps in magnetic data interpretation (Figure 8b).

320

321
322
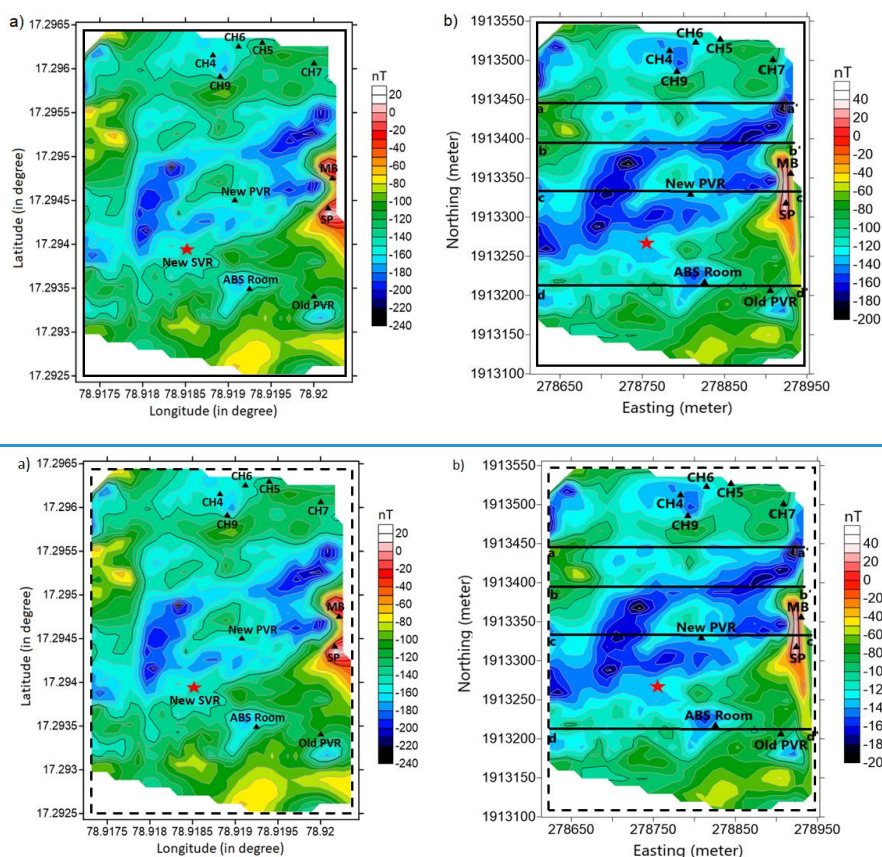
Figure 8: a) The magnetic anomaly of the study area. (MB=main building, SP= solar panel, CH= bore well channels, ABS= absolute, PVR= primary variometer room, SVR= secondary variometer room). Red star mark shows the proposed New SVR in the region, b) the magnetic anomaly after reduction to equator of the study area. The aa', bb', cc' and dd' shows four magnetic profiles modelled.

The RTE magnetic anomaly shows a variation of ~ 260 nT in the region. The low anomaly is dominant in the central part followed by the high anomaly near the main building and solar panel. The new PVR lies in the low anomaly region where the three-axis flux magnetometer is installed to record 1-sec H, D, and Z component data of Earth's magnetic field. The ABS room location is set up in the low anomaly zone to

measure the Delineation-Inclination using the Mag-01 DI-fluxgate magnetometer mounted on theodolite.

We have considered four profiles aa', bb, cc', and dd' along EW in the RTE magnetic anomaly map to characterise the subsurface susceptibility model (Figure 8b). The magnetic data shows its importance in characterizing the shallow sub-surface structures, which would be further beneficial for the selection of new location to install magnetic observatory in the campus. The lightning data is considered from the National Remote Sensing Centre (NRSC), Hyderabad, India, to investigate the failure of the DFM (digital fluxgate magnetometer) electronics during the lightning strike. The high-resolution topography data is obtained from the Shuttle Radar Topography Mission (SRTM) Global 30 (https://earthexplorer.usgs.gov/) to plot the elevation of the region.

The ERT surveys for different profiles (AA', DD', EE', FF' and GG') were carried out using Wenner and Schlumberger arrays with 48 electrodes in the campus. The profiles AA', DD', EE' with 5 m unit electrode spacing achieved a maximum length of 360 m whereas FF' and GG' covers 240 m (Maurya et al, 2021). The vertical cross section along these profiles and a horizontal depth slice at a depth of 30 m below ground level derived from 3D model reflect few linear conductive features and surficial resistivity heterogeneities (Figure 13a). The details about these surveys and results can be seen in Maurya et al., (2021).

359 **ii)   Analysis of subsurface source and depths**

360 The fast Fourier transform (FFT), a robust technique is used by several researchers

361 to calculate the mean depth of layered interfaces of the potential field datasets

362 (Chamoli et al., 2011, 2023; Dwivedi et al., 2019). The power spectrum analysis gives

363 the average depth of the sources with an error limit of 10% (Mishra and Pederson,

364 1982). The 2D radially averaged power spectrum of the RTE magnetic anomaly data

365 shows two linear slope segments corresponding to the average depth of two interfaces

366 around 12±1.2 m and 1±0.1 m (Figure 9).

367
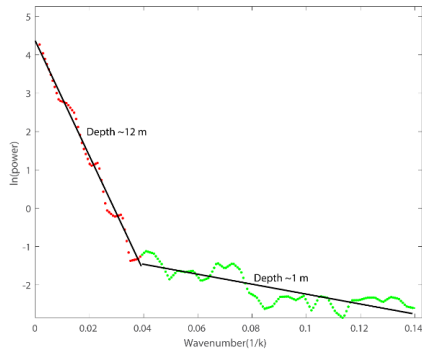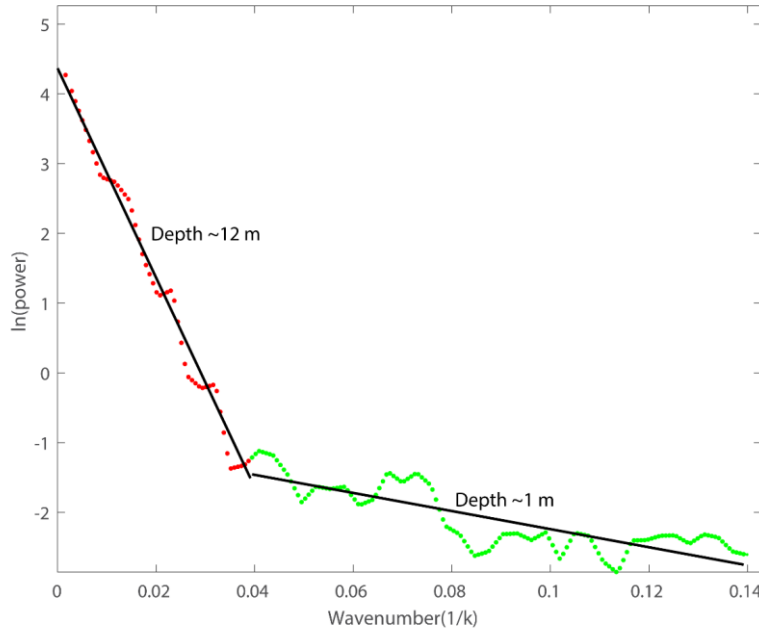
Figure 9: Radially averaged power spectrum of the RTE magnetic anomaly. Different layer segment give an average depth of layered interfaces.

370

The tilt depth is an effective method in characterizing the location of source edge as well as magnetic source depth using the tilt angle (TDR) approach (Salem et al., 2007). First, the TDR is described by the following equation (Miller and Singh, 1994).

$$\theta = tan^{-1}\left[\frac{\frac{\partial M}{\partial z}}{\sqrt{\left(\frac{\partial M}{\partial x}\right)^2 + \left(\frac{\partial M}{\partial y}\right)^2}}\right] \tag{1}$$

where $\frac{\partial M}{\partial x}, \frac{\partial M}{\partial y}, \frac{\partial M}{\partial z}$ are the first derivative of the magnetic field M in the x, y and z directions. The zero contour ($\theta = 0^0$) demarcates the spatial location of magnetic source and tilt amplitudes restrict in the range of $+90^0$ to -90^0. Salem et al., (2007)

378   introduced the tilt depth technique using the relationship among tilt angle (θ), depth

379   (Z_c), horizontal location (h) of a contact as:

380     $\theta = tan^{-1}\left[\dfrac{h}{Z_c}\right]$ (2)

381   In the equation 2, the contact location (h =0) lies to the zero values of the contour and

382   depth relates to the horizontal distance between the 0^0 and $\pm45^0$ contour in the TDR

383   map. We apply the technique to generate the tilt angle (TDR), tilt depth solution and

384   histogram plot on the magnetic gridded data. Figure 10 presents the TDR map with

385   displaying of contours of -45°, 0°, +45° (dashed black lines). The TDR shows the short

386   wavelength anomalies and closely spaced contours that corresponds to shallow sub

387   surface sources. The zero contour values of the TDR show the location of the source

388   whereas the half of the distance between $\pm45°$ contours demarcates depth of the

389   sources. It can be seen that distance between $0°$ and $+45^0$ is demarcated by relative

390   closeness over the shallow sources and wide expanses over the deeper sources.

391

392

393

394

395
396
397
398
399
400
401
402
403
404
405
406
407
408
409
410
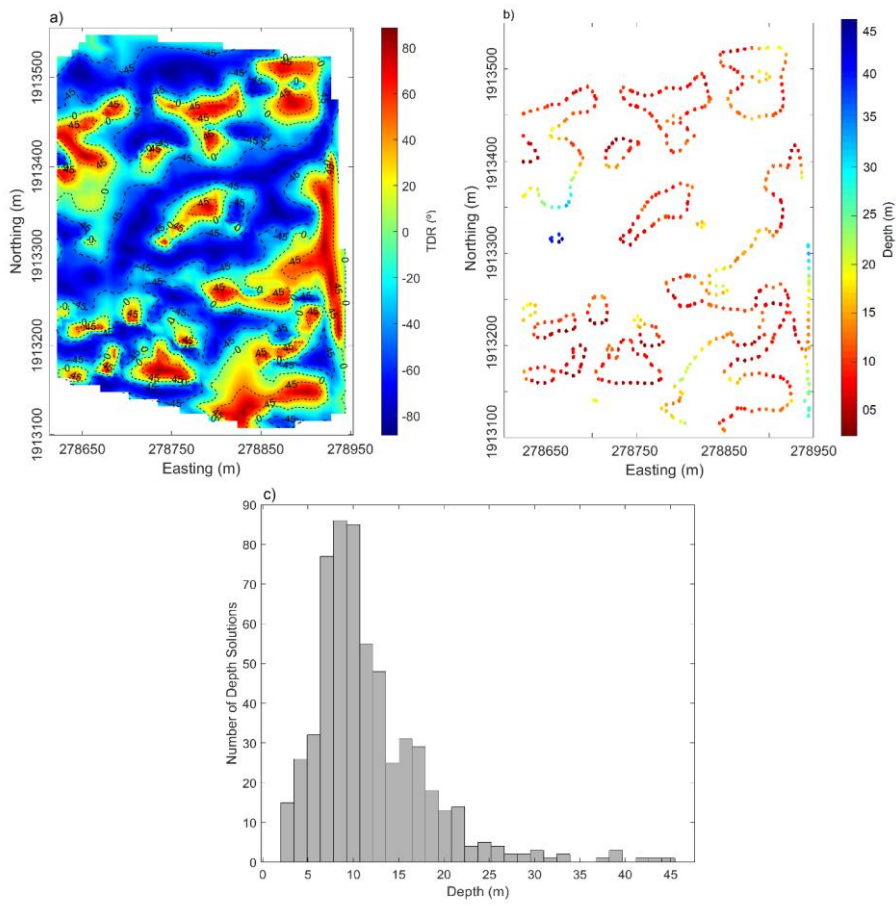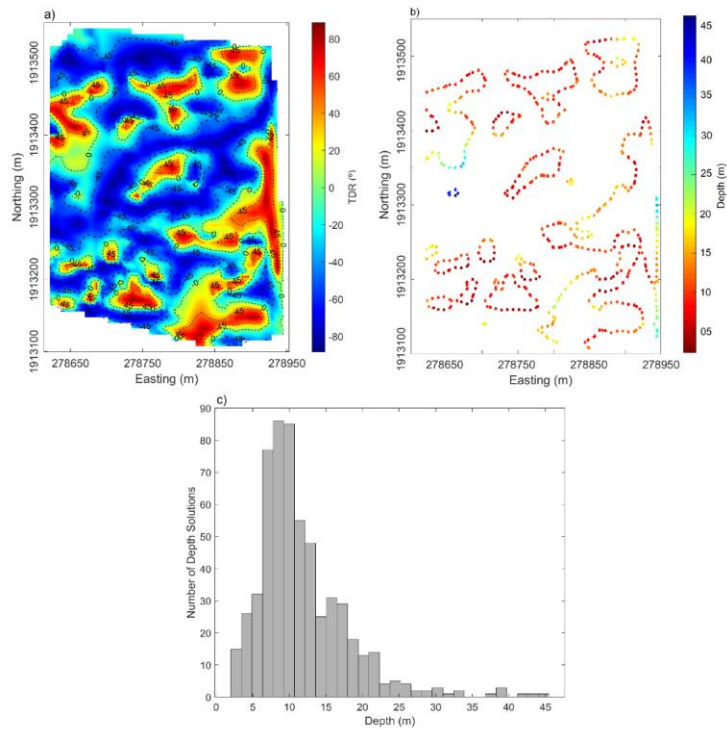
Figure 10: a) The tilt angle plot, b) The tilt depth solutions, c) the tilt depth solution histogram plot of the RTE magnetic anomaly.

The tilt depth solutions of the RTE magnetic anomaly data with depth variation from ~ 2 m to 45 m. Most of the sources lie in shallow depth ~ 2 to 20 m and extended in one direction. The histogram plot shows the variation between number of depth solution and depth (Figure 10c). It is clear from the plot that number of depth solution are maximum in the depth range of ~ 2 m to 20 m which corresponds to shallow source in the sub surface.

iii) Magnetic data inversion and forward models

We invert the RTE magnetic anomaly to estimate the depth variation of the interface with strong susceptibility contrast. We use the method of Parker (1973~~2~~) which works in the Fourier domain to estimate the depth variation of an undulated interface. The depth of interface can be computed from the magnetic anomaly due to an uneven, uniform magnetized layer by inversion procedure. The method is improved by incorporating high cut filter to ensure the convergence of series and to avoid instability at high wavenumber (Pham et al., 2020). Based on the power spectrum characteristics, we have chosen the cut-off wavenumber between 0.038-0.13 m^{-1} to remove the high frequencies. The resultant map shows that this interface is deepest in the centre of the survey area and shallowest towards the edges; then present PVR and the ABS Room are in the zones where this interface is deep, whereas the old PVR, which was flooded was in the zone of shallow interface (Figure 11a). The calculated depth is inferred as the saprolite layer, which varies from ~ 12 to 16 m with a mean depth of ~14 m. Figure 11b shows the variation of the root mean square (RMS) error against the iteration number. In this case, the inversion process performed 175 iterations, and the RMS error between two successive approximations was reduced from 0.0680 m to 9.9584×10^{-5} m.

472

473
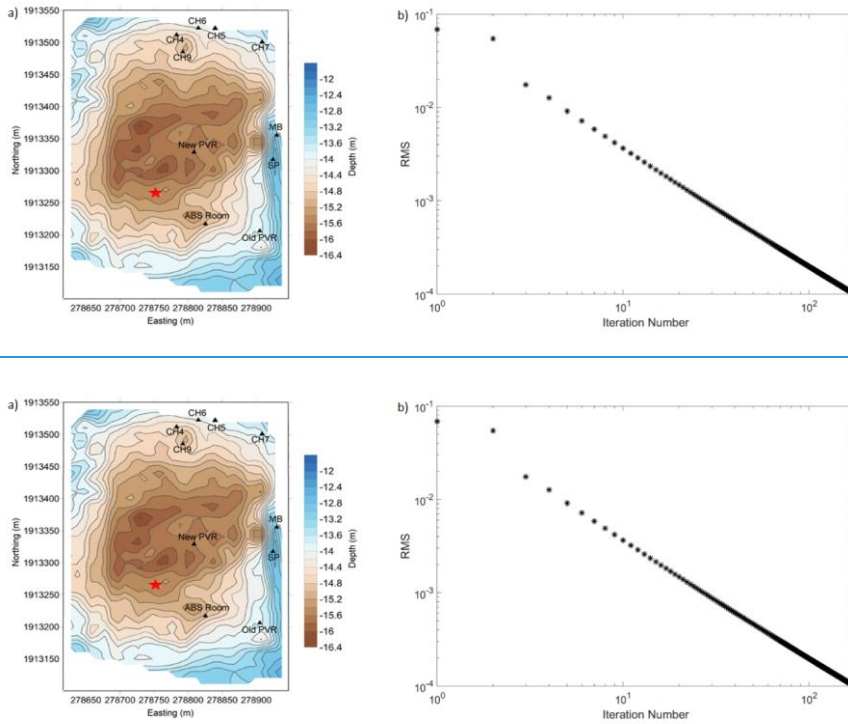
Figure 11: a) The depth variation of the saprolite interface derived from the inversion of the RTE magnetic anomaly after removing the high frequency component, b) variation of RMS error against the iteration number.

Further, we model the RTE derived magnetic anomaly data along four profiles aa', bb', cc', and dd' (Figure 8b) to delineate the details of the sub-surface structures. The forward modelling along these profiles is carried out using the IGMAS+ software, a tool for forward and inverse modelling of potential field datasets (Anikiev et al., 2023). The total length of theses profiles are ~310 m which show the depth variations up to 50 m from the surface (Figure 12a~~ 12d~~). The 2D models along these profiles explains the presence of three layered structures from the surface up to a depth of 50 m as: sandy regolith (~0.3 susceptibility in SI), saprolite (~3 susceptibility in SI), and fissured granite (~2.5 susceptibility in SI). The average susceptibility value for sandy regolith

488   layer is measured in the field using KT-10 magnetic susceptibility meter whereas

489   others are referenced from Telford et al., (1990). The saprolite interface is incorporated

490   in the models based on previous results of ERT data (Nicolas et al., 2019). The

491   average thickness of the sandy regolith layer is ~3 m whereas the saprolite layer is ~

492   10 m in the models. Both the saprolite and regolith layers show undulations in the all

493   models.

494

495

496

497

498

499

500
501
502
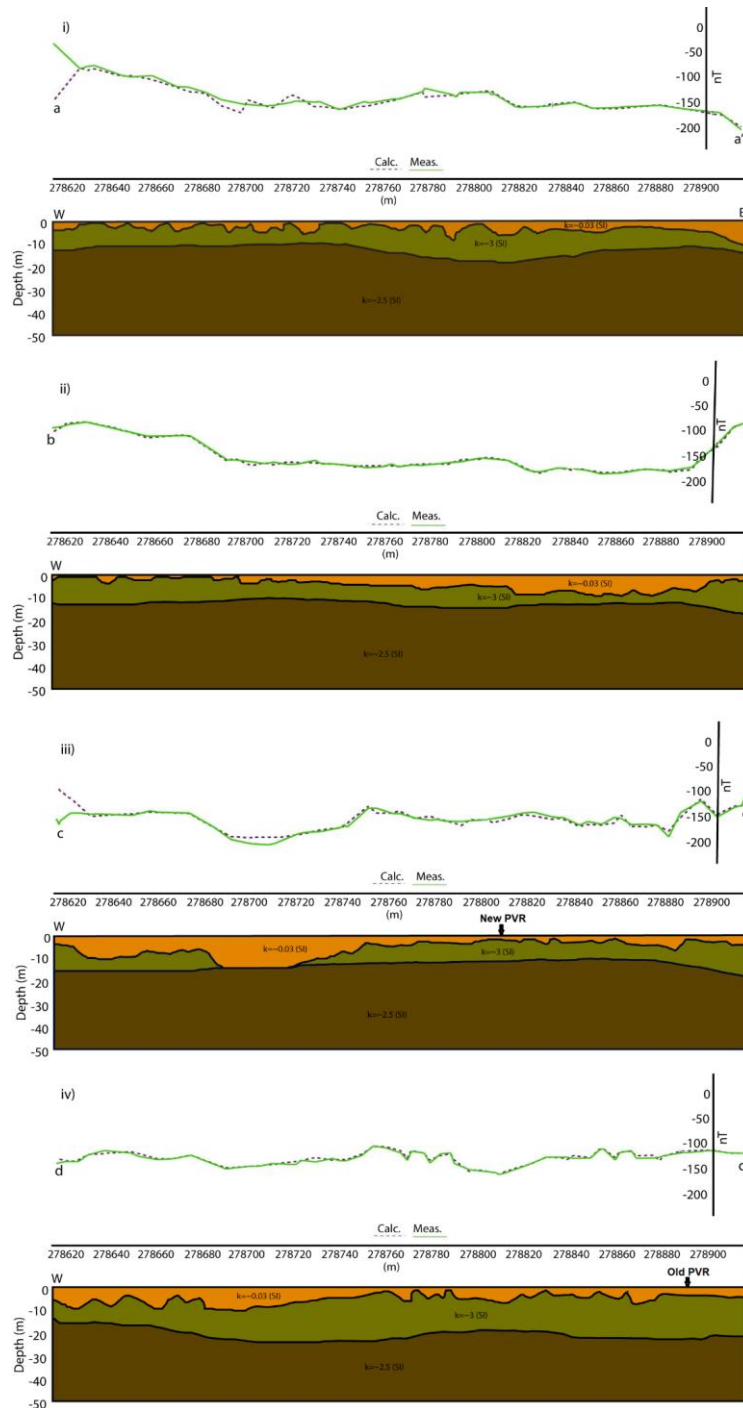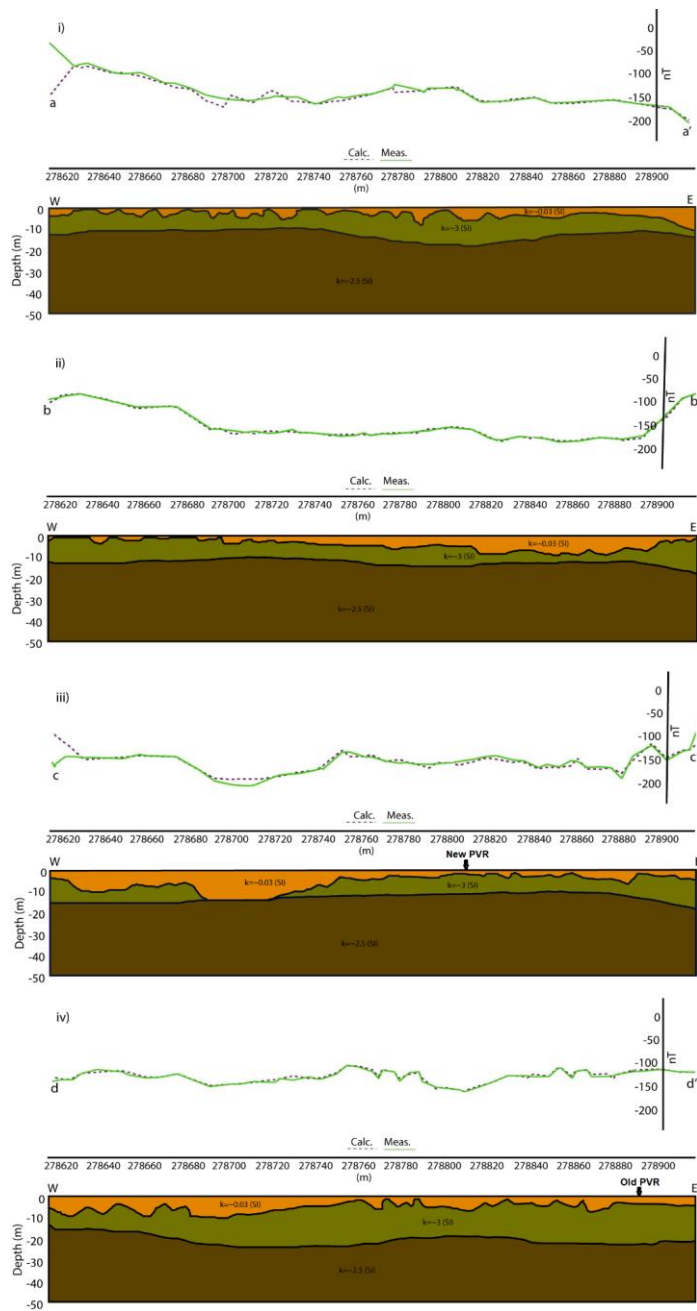
Figure 12: Magnetic data modelling across the profiles i) aa', ii) bb', iii) cc' and iv) dd' incorporating constrain from power spectrum, and past ERT studies. Top, middle and bottom layers in the models are sandy regolith, saprolite and granitic basements. The marked arrows show the location of New and Old PVR in profile cc' and dd'.

554
555
556   **iv)   Correlation with conductivity data/information**
557
558   The cc' magnetic profile is close to the vertical resistive cross-section along AA' of

559   Maurya et al., (2021) where resistivity increases from surface to depth (Figure 13a).

560   The old surface and apparent resistivity data of the region is digitized from the Sanker

561   Narayan et al., (1967) and overlaid over the topography (Figure 13b, 13c). The

562   apparent resistivity shows lateral varying high resistivity outward~~side~~ and vice-versa

563   inside the Choutuppal campus (Figure 13c). This indicates that conductivity decreases

564   outward, highlighting the presence of conductive soil layers within the campus.

565   ~~This means that conductivity decreases away and reflects the presence of conductive~~

566   ~~soil inside the campus.~~

567

568   The calculated saprolite depth by inverting magnetic data at different locations are ~

569   15.5 m (new PVR), ~ 15 m (ABS Room and CH9), ~ 13 m (MB and SP), ~14 m (old

570   PVR, CH5, CH6, CH7), ~ 14.5 m (CH4) (Figure 11a). Whereas, depth estimation by

571   the ERT data are ~ 13.5 m (new PVR), ~ 18 m (ABS Room), ~ 15 m (CH9), ~ 14 m

572   (MB, SP and CH4), ~22 m (old PVR and CH6), ~ 29 m (CH5) ~ 17 m (CH7)

573   respectively (Figure 13e). The calculated depth from these two different datasets show

574   a discrepancy of ~ 2m except at the locations of CH5, CH6 and old PVR. The ERT

575   survey estimates the upper fissured layer depth (~ 9 to 33 meters) of the Choutuppal

576   campus and shows the undulated interface creating compartmentalised aquifers

577   (Nicolas et al., 2019).

578
579
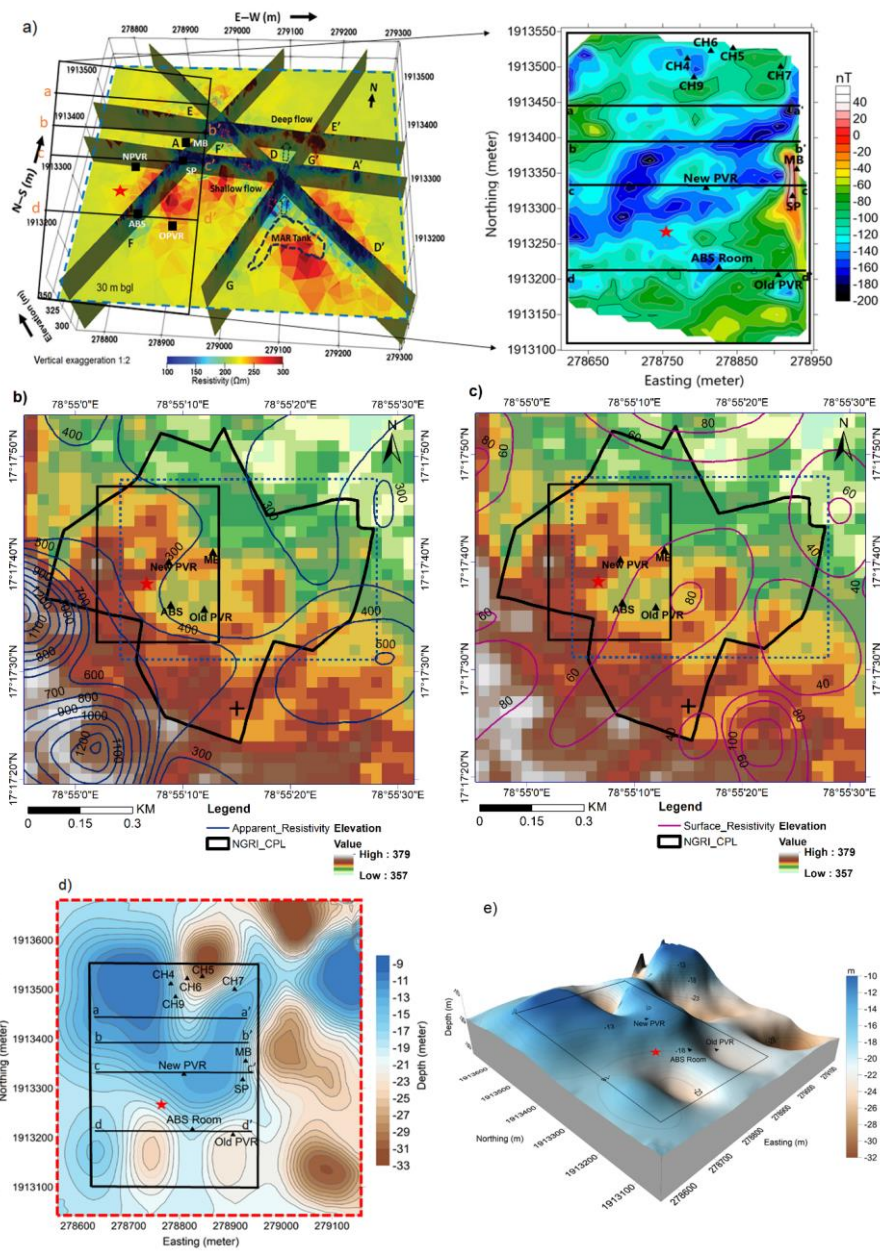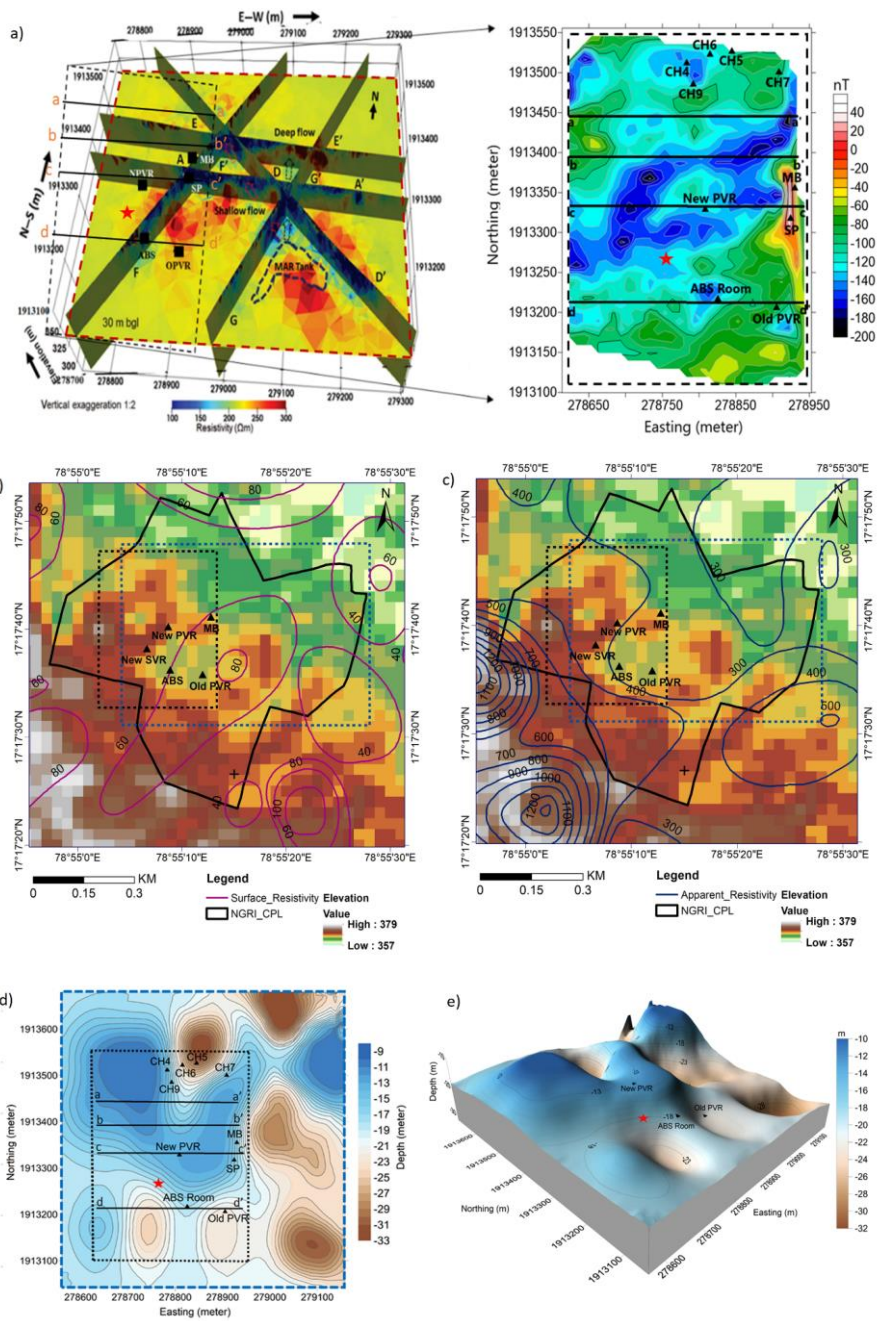
Figure 13: a) A resistivity model of the 2019 profiles along AA', DD', EE', FF', and GG' and a depth slice at 30m below ground level (after Maurya et al., 2021), b) ~~surface~~ apparent resistivity, c) ~~surface~~apparent resistivity superimposed over the topography with lightning strike location (+× symbol, intensity of 23208 amp. at a distance of 400 m from the MB on 04th May, 2022), d) depth estimation of saprolite interface from ERT data (after Nicolas et al., 2019), e) 3D view of saprolite interface ~~from figure 13d~~. The blue and red dotted rectangles represent the areas corresponding to the resistivity model and the saprolite interface, respectively, while the black rectangle highlights the magnetic anomaly region.
~~The blue dotted lines is the area correspond to resistivity model of 2019. Dashed black line shows the magnetic anomaly region.~~

5. Discussion and conclusion: proposed optimal location for SVR

The high resolution magnetic data provide a detailed shallow sub-surface structure at the CPL observatory. The power spectrum result shows two segments at a depth of ~ 12 m and ~1 m corresponding to saprolite and sandy regolith interface. These depths are similar to the previous depth estimated using the drilling data by Dewandel et al., (2006). The inversion results show the depth variation of the saprolite interface ~ 12 to 16 m (Figure 11a) which underestimate with the upper fissured layer depth from the ERT survey (Figure 13d). The obtained interface shows depression in the central region of the map with crests in the outer region and linear variation in depths (Figure 11a). The estimated depths at different locations shows ~ 2 m differences from these two datasets except at the location of CH5, CH6 and old PVR. These discrepancies in the depths estimation may be due to measurements of two different independent physical parameters susceptibility and conductivity. The saprolite interface might be delineate better by the ERT data due to presence of significant resistivity contrast between saprolite and granitic bedrock in the region (Robinson et al., 2008; Gourdol et al., 2021). The tilt depth plot of the anomaly data reflects depth variation from ~ 2 m to 45 m (Figure 10b). The histogram plot confirms the presence of the shallow sources in the depth range of ~ 2 m to 20 m based on the majority of a number of depth

solutions (Figure 10c). These shallow sources are in circular and elongated shapes which may be residue of igneous intrusion (Gorczyk and Vogt, 2018). At shallow depths, circular bodies with a magnetic contact source might produce symmetric anomalies in the magnetic data (Hinze et al., 2013). In contrast, elongated bodies may produce linear magnetic anomalies that follow the direction of the body as in the present study.

The sub-surface susceptibility models along the magnetic profiles aa', bb', cc', and dd' reflect the geometry of sandy regolith, saprolite layer and basement fissured granite (Figure 12). The saprolite layer shows undulating variation with quiet thick and thin at different locations along the profiles. These variations illustrate that the saprolite layer is thin in the region where the anomaly is low and it shows the thickness in the region where the anomaly is high. The magnetic anomaly shows a large depression of length ~ 80 m in the profile cc' (Figure 12c) where saprolite layer is absent and this depression arises due to sandy layer in the model. The 3D cross-sectional resistivity model infers the presence of high conductive anomalies followed by the moderate conducting saprolite layer and the low conductive basement rocks (Figure 13a).

Figure 13c shows that the apparent resistivity increases laterally outward, indicating the presence of highly conductive soil layers within the campus Figures 13c and 13d show that the apparent resistivity increases laterally away from the campus and shows the presence of high conductive soil layers inside the campus (Sanker Narayan et al., 1967). The apparent and surface resistivity demonstrate the linear relationship with the topography. The comparison between the latest resistivity model (~200 Ωm variation) for 2019 profiles (Figure 13a) and the old apparent resistivity (~300 Ωm

640 variation) plot in 1964 (Figure 13c) shows the resistivity change of ~100 Ωm. This

641 discrepancy may be due to the presence of newly constructed artificial recharge pond

642 which may decrease the resistivity due to its high conductive nature. The thin saprolite

643 layer may be associated with high electrical conductivity, which can result in a low

644 magnetic anomaly, and vice versa. The thin saprolite layer corresponds to high

645 conductivity, which gives low anomaly of the magnetic data and vice versa. Overall,

646 the resistivity variation increases from surface to greater depth. The resistivity model

647 also show that the artificial recharge pond has good subsurface connectivity, helping

648 the groundwater recharge towards the north and northwest directions in the campus

649 (Maurya et al., 2021). The water level started to rise in June-2016 and reached to very

650 shallow depth in channels during December 2017. It is evident that since last half of

651 2016, the recharge has led to saturation, which transformed the hydrogeological

652 regime of the campus. This may also cause a partial change in the rock magnetism

653 due to water saturation (Csontos et al., 2019) resulting in a decrease in the magnetic

654 anomaly (Figure 4a, 8a). The rainfall of 2017 monsoon combined with the already

655 prevalent saturated conditions led to the flooding of the magnetometer vault. The

656 location of new PVR has advantages as it is away from the water recharge pond,

657 minimal magnetic gradient anomaly but generation of induced current in the rainy

658 seasons due to presence of conductive environment around the location.

659

660 The effect of lightning strikes on the data with increasing distance, intensity and ground

661 conductivity shows that higher intensity strikes has had an impact of the data and

662 instruments.

663

Based on the above it is very crucial to determine the location and configuration where the installation can avoid the effects of groundwater fluctuations as well as lightning strikes, based on the nature of subsurface rocks, soil conditions, and their magnetic variations. The susceptibility model along with ~~conductivity~~ resistivity information are used to make a selection of a new SVR~~site~~ (78.9185E, 17.2939N)~~for trial measurements~~, indicated by red star in Figures 1, 8, 11, 13. This location is on low magnetic anomaly of ~ -145 nT (Figure 8a), resistivity ~200 Ωm (Figure 13a), moderately high ground ~367 m (Figure 13b), and depth of saprolite layer~~te~~ ~ ~~is about~~ 20 m (Figure 13d)~~conductivity in range of 200 Ωm, magnetic gradient of ~20 nT~. A thicker saprolite layer can enhance the resistive environment and reduce current propagation. The location's sufficient distance (~ 320 m) from the recharge tank ensures that water infiltration is unlikely to pose a significant issue. It is proposed that the pillar will be constructed within a semi-underground vault, in order to minimize the influence of induced currents during rainy seasons and lightning strikes. Additionally, the volume surrounding the pillar should be filled using high-resistivity material, such as Quartzite, to further minimize the likelihood of induced currents during lightning events or wet conditions.

~~It is proposed to construct the pillar in a semi-underground vault below regolith level, to avoid additional currents during the rainy season as well as during lightning strikes. The surrounding area around the pillar should be completely resistive to minimize the generation of these induced currents. The more thickness of saprolite may create resistive environment in the region and water may also not create problem due to away from the recharge tank due to sufficient distance.~~

Acknowledgements:

689 We thank the Director, NGRI, for supporting the work; reference no.

690 NGRI/Lib/2025/Pub-35. The authors are thankful to Dr. Subhash Chandra and other

691 colleagues from the ground water department of CSIR-NGRI for providing the bore

692 well water level data and resistivity results. We also thank Dr. Phani Chandrasekhar

693 and Dr. Rahul Prajapati for help towards the repeat surveys.

694

695 **Authors' contributions:**

696 **DD:** Conceptualization, Methodology, Computation and Modeling, Formal analysis,

697 Writing-original draft and editing

698 **SY:** Data Processing, Modeling

699 **KA:** Conceptualization, Validation, Review and final editing

700 **RM:** Lightning data analysis, maps and figures

701 **AT:** Lightning data, validation

702

703 **Declaration of Competing Interest:**

704 The authors declare that they have no competing financial interests or personal

705 relationships that could have appeared to influence the work reported in this paper.

706

707 **Funding:**

708 No funding was provided for this work.

709

710

711

712

713 **Availability of data and material**

714 The magnetic data associated with this research are available and can be obtained

715 upon the request from corresponding author. The topography data is obtained from

716 the Shuttle Radar Topography Mission (SRTM) Global 30

717 (https://earthexplorer.usgs.gov/). The lightning data can be accessed through the

718 ISRO - National Remote Sensing Centre, Hyderabad (https://bhuvan-

719 app1.nrsc.gov.in/lightning/).

720

721

722

723 **References:**

724 Anikiev, D., Götze, H.-J., Plonka, C., et al., 2023. IGMAS+: Interactive Gravity and

725 Magnetic Application System. GFZ Data Services.

726 https://doi.org/10.5880/GFZ.4.5.IGMAS.

727 Arora K., Chandrashakhar Rao K., Manjula L., et al., 2016. The new magnetic

728 observatory at Choutuppal, Telangana, India. Journal of Indian Geophysical Union,

729 Special volume-2, 67-75.

730 Arora K., Selles A., Manjula L., et al., 2017. CPL Magnetic Observatory: Groundwater

731 flooding and Relocation requirement. Technical Report No. NGRI-magObs-2017-946.

732 Chamoli A., Pandey A.K., Dimri V.P., et al., 2011. Crustal configuration of the northwest

733 Himalaya based on modeling of gravity data. Pure and Applied Geophysics 168 (5),

734 827–844.

735 Chamoli A., Rana S.K., Dwivedi D., et al., 2023. Crustal structure and fault geometries

736 of the Garhwal Himalaya, India: Insight from new high-resolution gravity data modeling

737 and PSO inversion. Tectonophysics, 859, 229904.

738 https://doi.org/10.1016/j.tecto.2023.229904.

Csontos A., Kónya P., Falus G., et al., 2019. Unstable spatial differences of the geomagnetic elements caused by changing water saturation of a volcanic sediment. Annals of Geophysics, 61(6), GM669. https://doi.org/10.4401/ag-7351

Dewandel B., Lachassagne P., Wyns R., et al., 2006. A generalized 3-D geological and hydrogeological conceptual model of granite aquifers controlled by single or multiphase weathering. Journal of Hydrology, 330, 260-284, https://doi.org/10.1016/j.jhydrol.2006.03.026.

Dewandel B., Maréchal J.C., Bour O., et al., 2012. Upscaling and regionalizing hydraulic conductivity and effective porosity at watershed scale in deeply weathered crystalline aquifers. Journal of Hydrology, 416–417, 83-97. https://doi.org/10.1016/j.jhydrol.2011.11.038.

Dwivedi D., Chamoli A., Pandey A.K., 2019. Crustal structure and lateral variations in Moho beneath the Delhi fold belt, NW India: Insight from gravity data modeling and inversion. Physics of the Earth and Planetary Interiors, 297, 106317. https://doi.org/10.1016/j.pepi.2019.106317

Dwivedi D., Chamoli A., 2021. Source Edge Detection of Potential Field Data Using Wavelet Decomposition. Pure and Applied Geophysics, https://doi.org/10.1007/s00024-021-02675-5.

Dwivedi D., Chamoli A., 2022. Seismotectonics and lineament fabric of Delhi fold belt region, India. Journal of Earth System Science, 131, 74. https://doi.org/10.1007/s12040-022-01829-w.

Gorczyk W., Vogt K., 2018. Intrusion of magmatic bodies into the continental crust: 3D numerical models. Tectonics, 37, 705–723. https://doi.org/10.1002/2017TC004738

Gourdol, L., Clément, R., Juilleret, J., et al., Pfister, L., and Hissler, C., 2021. Exploring the regolith with electrical resistivity tomography in large-scale surveys: electrode spacing-related issues and possibility. Hydrology and Earth System Sciences, 25, 1785–1812, https://doi.org/10.5194/hess-25-1785-2021, 2021.

Guihéneuf N., Boisson A., Bour O., et al., 2014. Groundwater flows in weathered crystalline rocks: Impact of piezometric variations and depth-dependent fracture connectivity. Journal of Hydrology, 511, 320–334. https://doi.org/10.1016/j.jhydrol.2014.01.061.

Hinze W.J., Von Frese R.R.B., Von Frese R., et al., 2013. Gravity and Magnetic Exploration: Principles, Practices, and Applications. Cambridge University Press, Cambridge.

Kumar R., Bansal A. R., Anand S. P., et al., 2018. Mapping of magnetic basement in Central India from aeromagnetic data for scaling geology. Geophysical Prospecting, 66, 226–239.

Maréchal J. C., Selles A., Dewandel B., et al., 2018. An observatory of groundwater in crystalline rock aquifers exposed to a changing environment: Hyderabad, India. Vadose Zone Journal, 17, 180076, https://doi.org/10.2136/vzj2018.04.0076

Maurya V.P., Chandra S., Sonkamble S., et al., 2021. Electrically inferred subsurface fractures in the crystalline hard rocks of an Experimental Hydrogeological Park, Southern India. Geophysics, 86(5), WB9-WB18, https://doi.org/10.1190/geo2020-0327.1

Maurya V.P., Gupta S.M., Mishra A., et al., 2024. Three dimensional electric field vector resistivity imaging for deep subsurface fractures network in heterogeneous crystalline rocks, Geophysical Journal International, 236 (1), 305-321, https://doi.org/10.1093/gji/ggad431

788 Miller H. G., Singh V., 1994. Potential field tilt-a new concept for location of potential

789 field sources. Journal of Applied Geophysics, 32, 213–217.

790 Mishra D., Pedersen L.B., 1982. Statistical analysis of potential fields from subsurface

791 reliefs. Geoexploration, 19, 247–265. https://doi.org/10.1016/0016-7142(82)90030-8.

792 Nicolas M., Bour O., Selles A., et al., 2019. Managed Aquifer Recharge in fractured

793 crystalline rock aquifers: Impact of horizontal preferential flow on recharge dynamics.

794 Journal of Hydrology, 573, 717-732, https://doi.org/10.1016/j.jhydrol.2019.04.003.

795 Parker R., 1973. The rapid calculation of potential anomalies. Geophysical Journal

796 International, 31 (4), 447-455, https://doi.org/10.1111/j.1365-246X.1973.tb06513.x

797 Pham L.T., Oksum E., Gómez-Ortiz D., et al., 2020. MagB_inv: A high performance

798 Matlab program for estimating the magnetic basement relief by inverting magnetic

799 anomalies. Computers & Geosciences, 134,104347,

800 https://doi.org/10.1016/j.cageo.2019.104347

801 Reynolds J., 1997. An Introduction to Applied and Environmental Geophysics, Wiley,

802 Chester, 2nd edition, 710p.

803 Robinson D. A., Binley A., Crook N., et al., 2008. Advancing process-based

804 watershed hydrological research using near-surface geophysics: A vision for, and

805 review of, electrical and magnetic geophysical methods, Hydrological Processes, 22,

806 3604–3635, 2008.

807 Salem A., Williams S., Fairhead J., et al., 2007. Tilt-depth method: a simple depth

808 estimation method using first-order magnetic derivatives. Leading Edge 26, 1502–

809 1505.

810 Sanker Narayan, 1964. Establishment of a magnetic observatory at NGRI. Bull NGRI,

811 2, 115-122.

812 Sanker Narayan P.V., Ramanujachary K.R., Sarma S.V.S., et al., 1967. Establishment

813 of a geoelectric observatory by the NGRI, Hyderabad, at Choutuppal, Nalgonda, Bull.

814 NGRI, 5, 155.

815 Sarma Y.S., Sanker Narayan P.V., Ramanujachary K.R., et al., 1969. Three component

816 induction magnetometer for recording geomagnetic micropulsations at the Geoelectric

817 observatory at Choutuppal, Bull. NGRI, 7, 51-65.

818 Spector A., Grant, F.S., 1970. Statistical models for interpreting aeromagnetic data.

819 Geophysics 35 (2), 293–302.

820 Svendsen, K.L., Davis, W.M., McLean, S.J., Meyers, H. 1990. A report on

821 geomagnetic observatory operations. NOAA, NGDC, Boulder, Colorado, USA.

822 Taori A., Suryavanshi A., Pawar S., et al., 2022. Establishment of lightning detection

823 sensors network in India: generation of essential climate variable and characterization

824 of cloud-to-ground lightning occurrences. Natural Hazards, 111, 19-32,

825 https://doi.org/10.1007/s11069-021-05042-8

826 Taori A., Suryavanshi A., Bothale R.V., 2023. Cloud-to-ground lightning occurrences

827 over India: seasonal and diurnal characteristics deduced with ground-based

828 lightning detection sensor network (LDSN). Natural Hazards, 116, 4037-4049.

829 https://doi.org/10.1007/s11069-023-05839-9

830

831 Telford, W. M., Geldart, L. P., Sheriff, R. E., 1990. Applied Geophysics (2nd ed.).

832 Cambridge: Cambridge University Press.

833 Tiwari V.M., Vyghreswara Rao M.B.S., Mishra D.C., et al., 2006. Crustal structure

834 across Sikkim, NE Himalaya from new gravity and magnetic data. Earth and Planetary

835 Science Letters, 247, 61-69, https://doi.org/10.1016/j.epsl.2006.03.037.